Non-Smooth Dynamics of Tapping Mode Atomic Force Microscopy

Belardinelli, Pierpaolo; Chandrashekar, Abhilash; Alijani, Farbod; Lenci, Stefano

DOI
10.1115/1.4062228

Publication date
2023

Document Version
Final published version

Published in
Journal of Computational and Nonlinear Dynamics

Pierpaolo Belardinelli[1]
Mem. ASME,
DICEA,
Polytechnic University of Marche,
Ancona 60131, Italy
e-mail: p.belardinelli@univpm.it

Abhilash Chandrashekar
PME,
TU Delft
Delft, The Netherlands
e-mail: a.chandrashekar@tudelft.nl

Farbod Alijani
PME,
TU Delft,
Delft, The Netherlands
e-mail: f.alijani@tudelft.nl

Stefano Lenci
Professor,
Mem. ASME
DICEA
Polytechnic University of Marche
Ancona 60131, Italy
e-mail: lenci@univpm.it

Non-Smooth Dynamics of Tapping Mode Atomic Force Microscopy

This study examines the nonlinear dynamics in tapping-mode atomic force microscopy (AFM) with tip-surface interactions that include van der Waals and Derjaguin-Müller-Toporov contact forces. We investigate the periodic solutions of the hybrid system by performing numerical pseudo-arclength continuation. Through the use of bifurcation locus maps in the set of parameters of the discontinuous model, the overall dynamical response scenario is assessed. We demonstrate the influence of various dissipation mechanisms that are related with the AFM touching or lacking contact with the sample. Local and global analyses are used to investigate the stability of the stable solution in the repulsive regime. The impacting nonsmooth dynamics framed within a higher-mode Galerkin discretization is able to capture windows of irregular and complex motion. [DOI: 10.1115/1.4062228]

1 Introduction

Atomic force microscopy (AFM) is one of the most prominent tool in nanotechnology [1,2]. When in tapping-mode operation, a sharply engineered tip at the free end of a microcantilever is brought via near-resonant excitation to interact with the sample. The shorter period of time the tip is in touch with the sample while using tapping mode AFM (TM-AFM) is a significant benefit. By reducing friction and adhesion with the specimen, the intermittent interaction minimizes the invasiveness [3,4]. Thus, the technique is suitable to get high-resolution topographical examinations of soft and fragile matter that are arduous to scan otherwise [5,6]. Beside imaging, thanks to a limited sample-damage, TM-AFM allows for the investigation of elastic/viscoelastic properties of polymers [7,8] and cells [9].

The forces that interact between the tip and the sample during tapping determine how the AFM cantilever behaves. The tip-sample interaction is inherently nonlinear and composed of long-range attractive, adhesive, short-range quantum repulsive and contact forces [10]. The interaction becomes even more complex when dealing with capillary forces [11]. Characterization of the intermittent contact in TM-AFM is essential in such a complex setting [12,13]; furthermore, this assumes additional significance since nonlinearities can be deftly exploited for identification purposes [14,15]. A number of different models and approaches have been used to reconstruct and investigates the AFM micro-cantilever oscillations [16–19]. A first group of studies employs a simplified single-degree-of-freedom point mass model [20]. Lumped models fail to describe completely the microcantilever subjected to base excitation as they do not capture parametric excitation components [13]. A continuous model is preferable to the point mass model when attempting to precisely characterize the dynamics of the microcantilever, despite the fact that it involves more complex modeling [21]. This approach offers more thorough understandings of the physics behind the nonlinear events such as amplitude jumps, period-doubling, and grazing bifurcations [22]. Literature presents single-degree-of-freedom reduced-order models using the Galerkin spectral projection [23]. The influence of higher modes of vibration in the nonlinear dynamics of AFM microcantilevers has recently come under scientific scrutiny [24]. As a matter of fact, when aiming to accurately measure the sample mechanical characteristics, additional observables could provide major insights [25]. AFM methods with many frequencies are being used to get around the single observable restriction [26]. In order to get complementary information about the interacting sample, these approaches primarily leverage higher harmonics of the cantilever deflection signal or the output signals of multiple resonant modes [27]. In this context, higher-flexural mode shapes can be used to build a multimodal Galerkin discretization which is able to capture more profound phenomena [22,28,29]. Thus, the first contribution of this article is to employ both the single-degree-of-freedom (SDOF) reduction and a multidegree-of-freedom (MDOF) approximation to establish how a basic or an augmented formulation intervenes in the description of the nonlinear dynamics. A multimode cantilever model together with tip-sample sample interaction governed by van der Waals and Derjaguin-Müller-Toporov (DMT) forces [30] is considered for the analysis. The piecewise formulation of the system is embraced by a well-defined algorithm that handles the hybrid dynamical description [11]. Under the hybrid formalism, we accurately resolve the dynamic stability of periodic responses with impacting behavior and the consequent switching between states [31].

We investigate the role played by governing parameters, emphasis is placed on critical values that potentially lead to dangerous loss of stability. While the effect of normalized coefficients on the frequency response (proportional to the sample elasticity, Hamaker constant and tip radius) has been previously investigated [32], damping effects remain largely unexplored. To date, a clear connection has not been presented upon the effects of the dissipation parameters and the hysteretic amplitude jumps. The second contribution of this paper is to explore the nonlinear response when varying the dissipation that occurs during the tip-sample interaction [33].

The paper is organized as follows. We begin presenting the continuous beam model used to predict the nonlinear AFM

[1]Corresponding author.

Manuscript received October 5, 2022; final manuscript received March 18, 2023; published online May 4, 2023. Assoc. Editor: Oumar Barry.

dynamics. The partial differential equation of motion is discretized through a Galerkin technique to obtain a set of nonlinearly coupled ordinary differential equations. Then, the model is rearranged in a hybrid system formulation. Numerical continuation performed by making use of the Computational Continuation Core toolbox (COCO) details a parametric analysis on the periodic cantilever oscillations [34]. The tool, which is ideally suited for our strongly nonlinear system, permits the continuation of both unstable and stable forced periodic solutions. It also detects the system bifurcations such as folds, period doubling, and torus bifurcations [35,36]. Finally, we study the bifurcations and the global dynamics in the case of a single and multimode approximation.

2 Mathematical Formulation

2.1 Tip–Sample Interaction. In order to investigate the TM-AFM dynamics, a force model F_{ts} is assumed to reconstruct the interaction between the microcantilever tip and the surface of the sample. The force is function of the instantaneous tip-sample separation z (see Fig. 1), which is described as follows [21]:

$$F_{ts}(z)=\begin{cases} F_{vdW}=-\dfrac{HR}{6z^2}, & \text{for } z>a_0 \\ F_{DMT}=-\dfrac{HR}{6{a_0}^2}+\dfrac{4}{3}E^*\sqrt{R}(a_0-z)^{3/2}, & \text{for } z\le a_0 \end{cases} \tag{1}$$

The tip-surface interaction is purely attractive when the separation distance z is larger than the intermolecular distance a_0 that represents the onset of the contact [10]. For small tip-sample distances, the attractive interaction F_{vdW} (Eq. $(1)_a$) arising due to long-range van der Waals forces is linear in the Hamaker constant H and in the tip radius R, whereas it is inversely proportional to the square of the separation distance. The strong repulsive DMT contact forces F_{DMT} [30] in Eq. $(1)_b$ are associated with the effective elastic modulus given by $1/E^*=(1-\nu_{tip}^2)/E_{tip}+(1-\nu_{sample}^2)/E_{sample}$, where E_{tip}, ν_{tip} are Young's modulus and Poisson's ratio of the cantilever tip while E_{sample}, ν_{sample} being those of the sample [4].

2.2 Equation of Motion. We write the dynamical equation for the AFM initially resting in a static equilibrium at a distance η^* from the sample as shown in Fig. 1. The mathematical framework to develop the continuous model for the AFM cantilever is within the Euler–Bernoulli assumptions. The AFM microcantilever has a length L, mass density ρ, Young's modulus E, area moment of inertia I, and cross section area A. The beam is clamped at $x=0$ and free at $x=L$. The microcantilever deflection is expressed in a noninertial reference frame attached to the base, considered excited with an harmonic motion $y(t)=Y\sin(\Omega t)$ via a dither piezo, where Y and Ω are the amplitude and frequency of excitation, respectively.

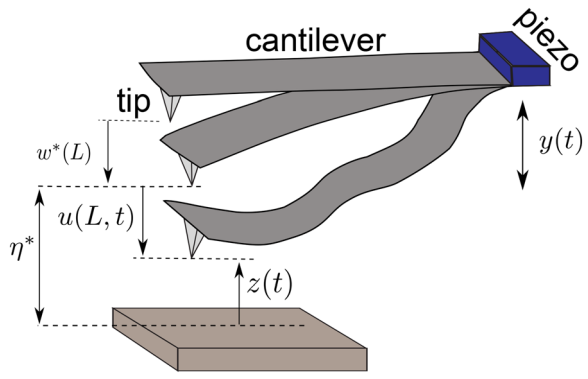

Fig. 1 A schematic of the AFM. Initially statically deflected configuration and dynamic configuration with the cantilever vibrating about its elastostatic equilibrium.

Thus, the instantaneous tip-sample distance is $z(t)=\eta^*-u(L,t)-y(t)$ where $u(x,t)$ is the dynamic deflection of the cantilever.

By indicating with $w^*(x)$ the static deflection written in the noninertial frame, the vibrations about the elastostatic equilibrium are governed by the equation [21]

$$\begin{aligned}&\rho A\ddot{u}(x,t)+\mathrm{EI}(u''''(x,t)+w^{*''''}(x))\\&=F_{ts}(z(t))\delta(x-L)+\rho A\Omega^2 Y\sin(\Omega t)\end{aligned} \tag{2}$$

Equation (2) is discretized through a projection onto linear mode shapes $\phi_i(x)$ computed around the microcantilever static configuration [22]. The response is approximated as

$$u(x,t)=\sum_{i=1}^{n}\phi_i(x)q_i(t) \tag{3}$$

with $q_i(t)$ being the generalized time dependent coordinate for the i-th mode of vibration. We substitute Eq. (3) in Eq. (2) and by utilizing the Galerkin procedure, we take the inner products with the same shape functions employed in the discretization. The final discretized dimensionless set of nonlinear ordinary equations reads

$$\ddot{\tilde{q}}_i+D_i(\bar{z})\dot{\tilde{q}}_i+K_i\tilde{q}_i=-C_i-F_{ts,i}(\bar{z})+B_i\bar{\Omega}^2\bar{y}\sin(\bar{\Omega}\tau) \tag{4}$$

where $\bar{z}$ is the dimensionless tip-sample separation distance given by

$$\bar{z}=1-\sum_{i=1}^{n}\tilde{q}_i-\bar{y}\sin\bar{\Omega}\tau \tag{5}$$

The system is subjected to the interaction force

$$F_{ts,i}(\bar{z})=\begin{cases} C_i/\bar{z}^2, & \text{for } \bar{z}>\bar{a}_0 \\ C_i/{\bar{a}_0}^2+G_i(\bar{a}_0-\bar{z})^{3/2}, & \text{for } \bar{z}\le\bar{a}_0 \end{cases} \tag{6}$$

After the spectral projection, the coefficients in Eqs. (4),(6) are

$$\begin{aligned}K_i&=\frac{{\omega_i}^2}{{\omega_1}^2},\quad C_i=-\frac{\mathrm{HR}\phi_i^2(L)}{6\rho A\eta^{*3}{\omega_1}^2\displaystyle\int_0^L\phi_i^2(x)dx},\\ B_i&=\frac{\phi_i(L)\displaystyle\int_0^L\phi_i(x)dx}{\displaystyle\int_0^L\phi_i^2(x)dx},\quad G_i=\frac{4E^*\sqrt{R\eta^*}\phi_i^2(L)}{3\rho A{\omega_1}^2\displaystyle\int_0^L\phi_i^2(x)dx}\end{aligned} \tag{7}$$

In the presented formulation, the generalized coordinates $\tilde{q}_i$ are normalized with value of the mode shape at the free end of the cantilever ($\tilde{q}_i=\phi_i(L)q_i$). The overdot in Eq. (4) means differentiation with respect to the dimensionless time, namely, $\tau=\omega_1 t$ where ω_1 is the fundamental frequency of the microcantilever. The amplitude and frequency of the excitation Y and Ω are related to their dimensionless counterparts through $\bar{y}=Y/\eta^*$ and $\bar{\Omega}=\Omega/\omega_1$, respectively. Finally, $\bar{a}_0=a_0/\eta^*$ is the dimensionless conjugate of the intermolecular distance a_0. Note that the modal damping $D_i(\bar{z})$ has been inserted in Eq. (4). As in Ref. [21], we consider a piecewise model that accounts for the dissipation mechanisms while the tip is in air ($\tilde{D}_i^{att}$) or in contact with the sample ($\tilde{D}_i^{rep}$):

$$D_i(\bar{z})=\begin{cases} D_i^{att}=\dfrac{\tilde{D}_i^{att}}{\omega_1\rho A\displaystyle\int_0^L\phi_i^2(x)dx}, & \text{for } \bar{z}>\bar{a}_0 \\ D_i^{rep}=\dfrac{\tilde{D}_i^{rep}}{\omega_1\rho A\displaystyle\int_0^L\phi_i^2(x)dx}, & \text{for } \bar{z}\le\bar{a}_0 \end{cases} \tag{8}$$

3 The Hybrid Dynamical System

In this section, we recast system of ODEs in the form of a *hybrid dynamical system*. Let $\boldsymbol{x} \in \mathbb{R}^{2n} \times \mathbb{S}^1$ be the state vector given by

$$\boldsymbol{x} = \begin{pmatrix} \{x_{2i-1}\}_{i=1}^{n} \\ \{x_{2i}\}_{i=1}^{n} \\ x_{2n+1} \end{pmatrix} = \begin{pmatrix} \{\tilde{q}_{2i-1}\}_{i=1}^{n} \\ \{\dot{\tilde{q}}_{2i}\}_{i=1}^{n} \\ \bar{\Omega}\tau \bmod 2\pi \end{pmatrix} \tag{9}$$

in which with the compact notation $\{\cdot\}_{i=1}^{n}$ is meant a vector subset. The in line full-form of the continuous state vector reads $\boldsymbol{x} = (x_1, x_3, \ldots, x_{2n-1}, x_2, x_4, .., x_{2n}, x_{2n+1})^T$. Here, the components x_{2i-1} and x_{2i} are the position and velocity of the i-th mode of vibration employed in the n-th order reduced-model. In addition, $x_{2n+1} \in [0, 2\pi)$ gives the instantaneous phase of the periodic forcing. In order to describe the AFM cantilever oscillations, the state vector $\boldsymbol{x}$ does not suffice. Indeed, it is necessary to know the instantaneous tip-sample interaction. The description of the active component (van der Waals or DMT) of the tip-sample interacting force is done by means of the discrete state variable k

$$F_{\mathrm{ts},i}(\bar{z}, k) = \begin{cases} C_i/\bar{z}^2, & k = 0 \\ C_i/{\bar{a}_0}^2 + G_i(\bar{a}_0 - \bar{z})^{3/2}, & k = 1 \end{cases} \tag{10}$$

When $k = 0$, i.e., $\bar{z} > \bar{a}_0$, the cantilever feels only attractive forces, while for $k = 1$, i.e., $\bar{z} \leq \bar{a}_0$, the tip experiences a constant attractive contribution of van der Waals and repulsive forces. Finally, in a similar fashion, we have defined the piecewise F_{ts}, and the active contribution for the damping can be disentangled through k by writing

$$D_i(k) = \begin{cases} D_i^{\mathrm{att}} & k = 0 \\ D_i^{\mathrm{rep}} & k = 1 \end{cases} \tag{11}$$

The piecewise smooth formulation of both F_{ts} and the damping brings to a hybrid (discontinuous) system where the continuous-time dynamics is halted by discrete-time events. The interrupting events are detected by looking for the zeros of user-defined event functions h (e.g., the zero-crossing of a threshold). At the event, the governing vector field can be held as it or be modified, although it remains smooth within each orbit chunk [34].

The exploration of the continuous-in-time response of the AFM cantilever in tapping-mode is provided by the set of first-order ODEs

$$\dot{\boldsymbol{x}} = \boldsymbol{f}(\boldsymbol{x}, k) = \begin{pmatrix} \{x_{2i}\}_{i=1}^{n} \\ \{-D_i(k)x_{2i} - K_i x_{2i-1} - C_i - F_{ts,i}(\bar{z}, k) + B_i\bar{\Omega}^2\bar{y}\sin x_{2n+1}\}_{i=1}^{n} \\ \bar{\Omega} \end{pmatrix}. \tag{12}$$

In order to visualize the trajectory of the cantilever in the phase-space, Fig. 2 reports two period-1 orbits for TM-AFM. When the AFM cantilever tip is not in contact with the sample, the dynamics occurs following the *no contact* segment

$$\dot{\boldsymbol{x}} = \boldsymbol{f}(\boldsymbol{x}, 0) = \begin{pmatrix} \{x_{2i}\}_{i=1}^{n} \\ \{-D_i^{\mathrm{att}}x_{2i} - K_i x_{2i-1} - C_i - C_i/\bar{z}^2 + B_i\bar{\Omega}^2\bar{y}\sin x_{2n+1}\}_{i=1}^{n} \\ \bar{\Omega} \end{pmatrix} \tag{13}$$

This is illustrated by the I_2 *no contact* segment in Fig. 2. The tip crossing the intermolecular distance a_0 terminates the segment. The contact event function h_c checks for the discontinuity boundary, i.e.,

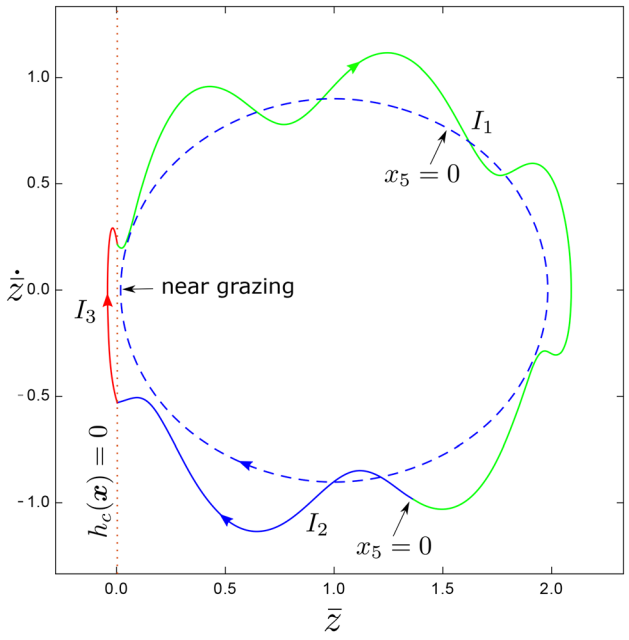

Fig. 2 Period-one orbits of TM-AFM model. With solid line, an impacting orbit with the three joint segments: I_1 *no contact* segment reaching the phase reset (the phase reset condition is $x_5 = 0$), I_2 *no contact* segment and I_3 *contact* segment. A nonimpacting orbit approaching the grazing contact is shown with dashed line, i.e., $\dot{\bar{z}} = 0$ at $h_c(\boldsymbol{x}) = 0$. Simulations parameters: $n = 2$ in Eq. (12), $\bar{y} = 0.108$, $D_{1,2}^{\mathrm{att}} = 0.025$, $D_{1,2}^{\mathrm{rep}} = 4.0$, $\bar{\Omega} = 0.98$ (solid line), $\bar{\Omega} = 0.916$ (dashed line).

$$\sum := \{(\{x_{2i-1}\}_{i=1}^{n}, \{x_{2i}\}_{i=1}^{n}) \in \mathbb{R}^2 : h_c(\boldsymbol{x}) := \bar{z} - \bar{a}_0 = 0\} \tag{14}$$

The subsequent segment describes the motion when the intermolecular distance is surpassed (I_3 *contact* segment of Fig. 2)

$$\dot{\boldsymbol{x}} = \boldsymbol{f}(\boldsymbol{x}, 1) = \begin{pmatrix} \{x_{2i}\}_{i=1}^{n} \\ \{-D_i^{\mathrm{rep}}x_{2i} - K_i x_{2i-1} - C_i - C_i/{\bar{a}_0}^2 - G_i(\bar{a}_0 - \bar{z})^{3/2} \\ \quad + B_i\bar{\Omega}^2\bar{y}\sin x_{2n+1}\}_{i=1}^{n} \\ \bar{\Omega} \end{pmatrix} \tag{15}$$

A full cantilever orbit is partitioned into smooth segments in which the terminal point of one segment is sewed to the initial point of the next one. The connection between segments is made through a jump function g that allows for the redefinition of the state vector. If no jump is needed the identity function $g_{\mathrm{id}}(\boldsymbol{x}) = \boldsymbol{x}$ sets the initial point of the next segment as the last of the previous one. As an illustrative case, let us consider the end of the contact segment I_3 in Fig. 2. It ends with the intersection of the discontinuity boundary $\sum$. Here, the noncontact segment I_1 is sewed to I_3 via g_{id}. In order to constrain the phase of the periodic driving within $\mathbb{S}^1$[2] an additional event function is monitored, i.e., $h_{2\pi}(\boldsymbol{x}) := x_{2n+1} - 2\pi = 0$. Eventually, the phase is reset with the jump function $g_{2\pi} := (\{x_{2i-1}\}_{i=1}^{n}, \{x_{2i}\}_{i=1}^{n}, x_{2n+1} - 2\pi)^T$ that does not modify the mechanical state variable but defines a further orbital segment, namely, I_1 *no contact* segment reaching the phase reset as shown in Fig. 2.

It is worth to note that the specified signature, i.e., the ordered sequence of the segments, remains valid if the contact time is smaller than one period of the driving force.

[2] $\mathbb{S} := \mathbb{R}/2\pi$ is the quotient set on $\mathbb{R}$ where two numbers are equivalent if differ by a multiple of 2π [34].

3.1 Event Detection and Grazing Contact. It is possible to discern two different scenarios during the transition between segments, namely, transversal and tangential crossing. The bifurcation scenario is strongly correlated to steady-state orbits grazing contact on the onset of the system discontinuity [12]. For the transversal or nontangential case, we look for the zero crossing of the event function from positive to negative such that at the crossing time t^*

$$h_c(\boldsymbol{x}(t^*)) = 0 \tag{16}$$

and

$$\partial_{\boldsymbol{x}} h_c[\boldsymbol{x}(t^*)] \cdot \boldsymbol{f}[\boldsymbol{x}(t^*), k] < 0 \tag{17}$$

In the second scenario, the tangential event leads to

$$\partial_{\boldsymbol{x}} h_c[\boldsymbol{x}(t^*)] \cdot \boldsymbol{f}[\boldsymbol{x}(t^*), k] = 0 \tag{18}$$

Equation (18) represents the condition for the grazing contact with the event surface $\sum$ which for the AFM cantilever means to verify the event function $h_{\mathrm{GR}}(\boldsymbol{x}) := \dot{\bar{z}} = 0$ when crossing a_0. Dashed orbit in Fig. 2 depicts a nonimpacting orbit approaching the grazing contact.

4 Results

In this section, we present the numerical results obtained by coding the hybrid dynamical system in the Computational Continuation Core toolbox developed by Dankowicz and Schilder [34]. Within the wide set of parameters governing the dynamics we selected $\{\bar{\Omega}, \bar{y}, \{D_i^{\mathrm{att}}\}_{i=1}^n, \{D_i^{\mathrm{rep}}\}_{i=1}^n\}$ to perform our bifurcation analysis. For the numerical investigation we fix the cantilever and interaction properties to the values listed in Table 1.

Former approaches in literature did not evaluate properly the frequency response of the AFM and corresponding bifurcation points [22,29]. Indeed, it is not possible to estimate folds precisely with a brute force numerical integration of the ODEs as basins of attraction shrink reaching the fold. Thus direct numerical integration requires initial conditions that are difficult to guess unless computing all the basins of attraction for each value of the bifurcation parameter [37]. The issue is somehow similar to when one tries to reach saddles in experiments as one must face limitations due to noise-induce fluctuations [38].

Figure 3 shows the evolution of the resonance curve as a function of the driving frequency $\bar{\Omega}$. In the ordinate axis, we plot the minimum dimensionless separation between the tip and the sample $\min \bar{z}$. The periodic solutions stability (solid/dotted lines indicate stable/unstable response) is studied based on the Floquet theory [39]. The near-resonant forced response of Fig. 3 shows an initial softening induced by the attractive forces and subsequent hardening in contact nonlinear response, the so-called "amplitude-saturated branch" (panel (b) of Fig. 3). The softening effect is minor and limited in the proximity of the intermolecular distance (dotted orange line). For the configuration under investigation, the van der Waal forces are quite weak and do not induce strong bending of the

Table 1 Properties and dimensions of the cantilever [21]

Description	Dimensions
Length (L)	240 μm
Width (b)	64μm
Thickness (h)	2.1 μm
Tip radius (R)	20 nm
Density (ρ)	2300 kg m^{-3}
Effective elastic modulus (E^*)	10.4 GPa
Reference distance (η^*)	60 nm
Intermolecular distance (a_0)	2Å
Hamaker constant (H)	2.96×10^{-19} J

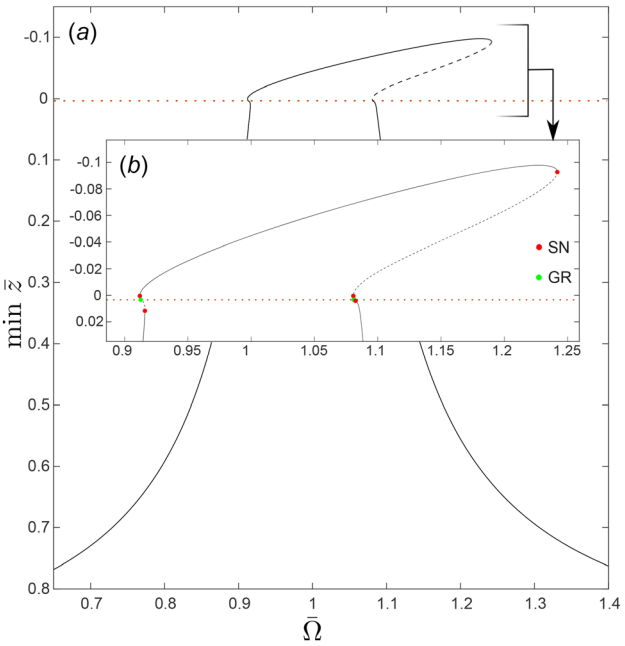

Fig. 3 The frequency response prediction obtained through continuation of periodic solutions in COCO. Panel (*a*) shows the complete bifurcation diagram for the minimum dimensionless tip/sample separation $\bar{z}$ as a function of the normalized frequency $\bar{\Omega}$. Dashed/Solid lines indicate unstable/stable solutions branches. The horizontal dotted line depicts the intermolecular distance a_0. Simulations parameters: $n = 1$, $\bar{y} = 0.108$, $D_1^{\mathrm{att}} = 0.025$, $D_1^{\mathrm{rep}} = 4.0$. Panel (*b*) zooms on the repulsive response region. Saddle-node (SN) and grazing (GR) bifurcations are indicated with red and green dots (darker and lighter in the hard copy), respectively.

curve. However, the softening response could be the prevailing factor in noncontact studies [14]. The frequency response manifests the coexistence of two stable oscillation states in TM-AFM. The two states are associated with the combined participation of attractive and repulsive forces, respectively. Multistable response is present below and above resonance although predominant in the amplitude-saturated response, which is typical during tapping mode operation. As shown in Fig. 3(*b*), the transition between attractive and repulsive is characterized by two saddle-node bifurcations (SN) that limits an unstable solution branch. At the crossing of the intermolecular distance, the sample exerts repulsive forces on the tip. The zoomed Fig. 3(*b*) shows the presence of additional saddle-type bifurcations induced by the presence of a grazing dynamics (GR) [40,41].

The frequency response of Fig. 3 represents the starting point for our bifurcation analysis. The study of bifurcations is a powerful tool that can be utilized for identification purposes. Recent examples are nonlinear dynamics-based identification of 2D materials [15] and, within the AFM realm, the estimation of tip radius by matching the softening nonlinearity in the noncontact regime [14]. In view of above, next we analyze the variation of bifurcations with respect to AFM key parameters.

4.1 Bifurcation Analysis of SDOF Model. In this subsection, an SDOF approximation is used, i.e., $n = 1$ in Eq. (9). The analysis concentrates on the repulsive amplitude-saturated response due to the intricacy and richness of nonlinear processes that emerge during the tip-sample interaction. Figure 4 reports loci for the main bifurcations occurring on the amplitude-saturated branch. Beside the translation of the saddle SN_1 toward larger values of $\bar{\Omega}$ and deeper sample penetrations (smaller $\min \bar{z}$), an increment of the excitation amplitude does not alter the global shape of the frequency response curve. Yet, this holds only for values of excitation amplitude $\bar{y} < 0.1252$ at which the stable manifold of the large oscillations in the repulsive regime is carved by period doubling bifurcations (PD). The destabilization of the nonlinear amplitude

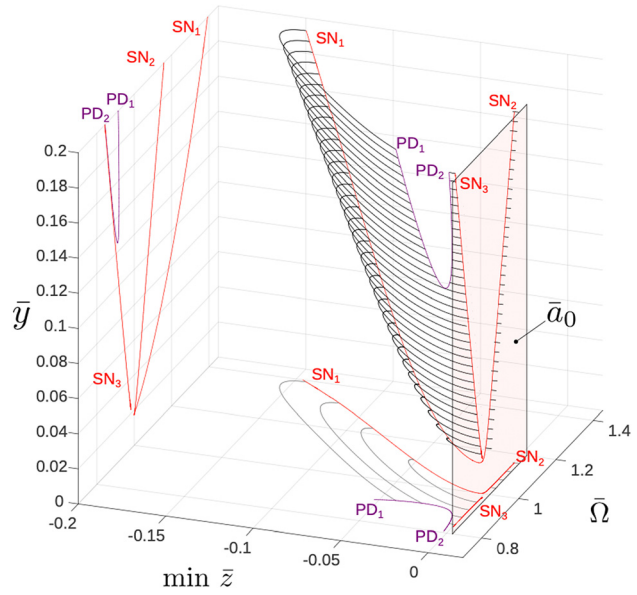

Fig. 4 Bifurcation diagram for the amplitude-saturated response. Bifurcation parameters: excitation amplitude $\bar{y}$, excitation frequency $\bar{\Omega}$. Red/Purple lines are saddle (SN)/Period doubling (PD) loci. Unstable branches are not reported. The transparent pink plane is the intermolecular distance plane.

response through period-doubling bifurcation is a severe problem while imaging with TM-AFM. Moreover, the microcantilever can eventually follow a cascade of PD bifurcations ending up with chaotic oscillations [42].

The bifurcation scenario outlined has a close relationship with the dissipation mechanisms. In fact, two distinct dissipation phenomena, in and out of contact (D_1^{rep} and D_1^{att}), govern the interaction between the tip and the sample. Their influence is detailed in Fig. 5. Panel (a) shows a three dimensional plot of the frequency response in the repulsive region. The figure helps to appreciate the significant change in reaction brought on by the dissipation in the out-of-contact zone (D_1^{att}). A first scenario (top frequency response in Fig. 5(*a*)) is represented by a cantilever heavily damped when far from the sample (e.g., $D_1^{\text{att}} = 0.04$). The reduced energy at the impact leads to a reduced penetration even while considering a low damped contact ($D_1^{\text{rep}} = 0.1$). In a second case, we observe the effect of highly-damped samples (e.g., $D_1^{\text{rep}} = 30$, lower frequency response in Fig. 5(*a*)). Here, the dissipation within the sample D_1^{rep} is the main mechanism preventing a marked penetration. The projection in Fig. 5(*b*) allows us to see how the response shape differs between the two scenarios. Large D_1^{rep} values bring to: (i) an increase of the saturation, i.e., flattening toward the intermolecular distance axis, of the repulsive branch; (ii) revert the concavity of the unstable solution branch; (iii) lose the stable solutions in proximity of the zero crossing and characterized by the points $SN_{2,3}$ (see Fig. 4 for reference). These effects are typical of hard materials as HOPG and MICA as reported in former experimental investigations [21]. The change in both slope and extension of the amplitude-saturated branch is vivid indication of the sensitivity to the sample properties. Mapping this susceptibility provides the ground for dynamical-based identification of specimens in the repulsive region.

In specific damping configurations, the microcantilever experiences the interaction with the sample (part of its oscillation remains beyond the intermolecular distance) but the upper saddle bifurcation disappears. Figure 5(*a*) highlights with a red line the position of the saddle node points SN_1 and SN_2 for the case scenario of Fig. 3 as function of D_1^{att} while keeping $D_1^{\text{rep}} = 4$ fixed. The two red loci join at the maximum of the red curve. Here, the value of the out-of-contact dissipation D_1^{att} is large enough to maintain the response stable for the entire frequency range. Accordingly, Fig. 6 provides a complete chart of the amplitude-saturated bifurcation by varying the damping in both attractive and repulsive region by fixing the locus of SN_1 to D_1^{rep} and D_1^{att}, respectively, and obtaining damping isolines. The figure gives a broad picture of how one source of dissipation compares to another. The saddle position is less susceptible to a variation in D_1^{rep} for strongly impacting cantilevers (low values of D_1^{att}) as reported in the right-lower part of Fig. 6(*a*). The response is characterized by flat and strongly amplitude-saturated branches. Figure 6(*a*) depicts a cusp catastrophe highlighted in the panel (*b*) in which the SN_1 manifold folds on itself.

4.2 Multidegree-of-Freedom Bifurcation Analysis. This section of the paper investigates the microcantilever dynamics of the

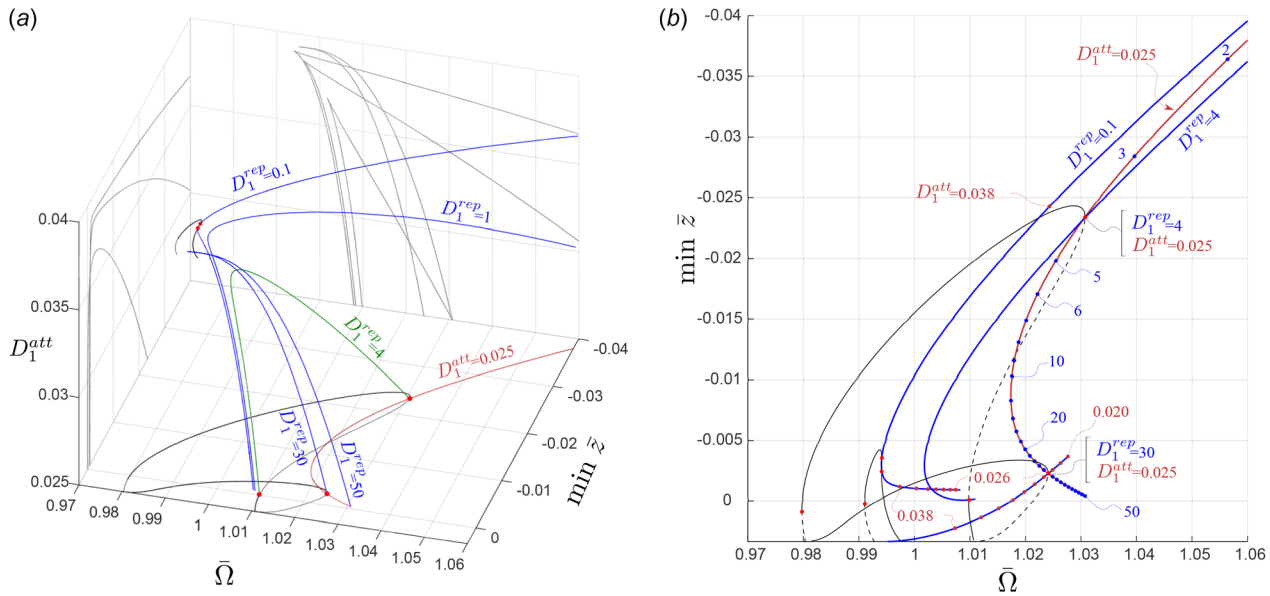

Fig. 5 Bifurcation diagram for the amplitude-saturated response as a function of the excitation frequency $\bar{\Omega}$. Excitation amplitude fixed at $\bar{y}$=0.108. Dark red/blue lines (light and dark colors in the hard copy) are the SN_1 loci for fixed $D_1^{\text{att}}/D_1^{\text{rep}}$. The line for $D_1^{\text{rep}} = 4.0$ is the locus of SN_1 and SN_2 for the case of Fig. 3. In panel (*a*), a three-dimensional plot shows the influence of D_1^{att}. The projection over the min$\bar{z}-\bar{\Omega}$ plane is reported in panel (*b*). In both (*a*) and (*b*) panels, the origin on the min$\bar{z}$ axis is at the intermolecular distance $\bar{a}_0$.

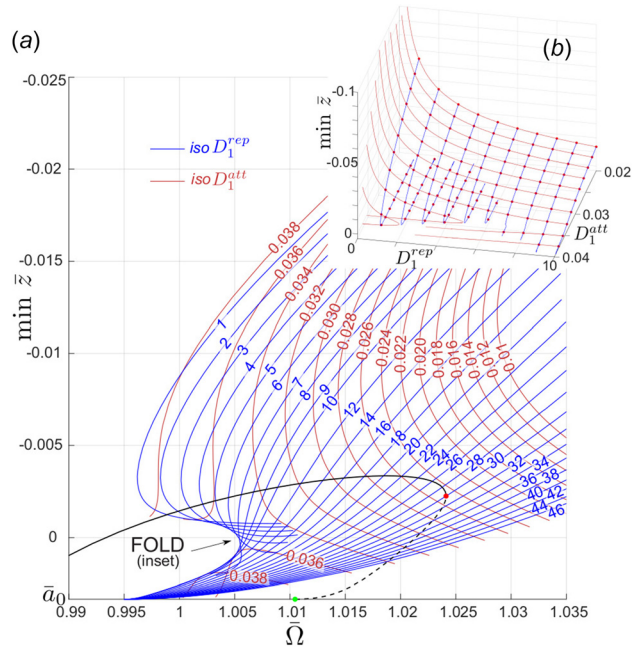

Fig. 6 Bifurcation diagram for the amplitude-saturated response as a function of the excitation frequency $\bar{\Omega}$. Excitation amplitude fixed at $\bar{y} = 0.108$. (*a*) Dark red/blue lines (light and dark colors in the hard copy) are the SN_1 loci for fixed D_1^{att}/D_1^{rep}. The position of the SN_1 in the case $D_1^{rep} = 30$ and $D_1^{att} = 0.025$ is reported for reference. The inset (*b*) enlarges the fold of the SN_1 manifold.

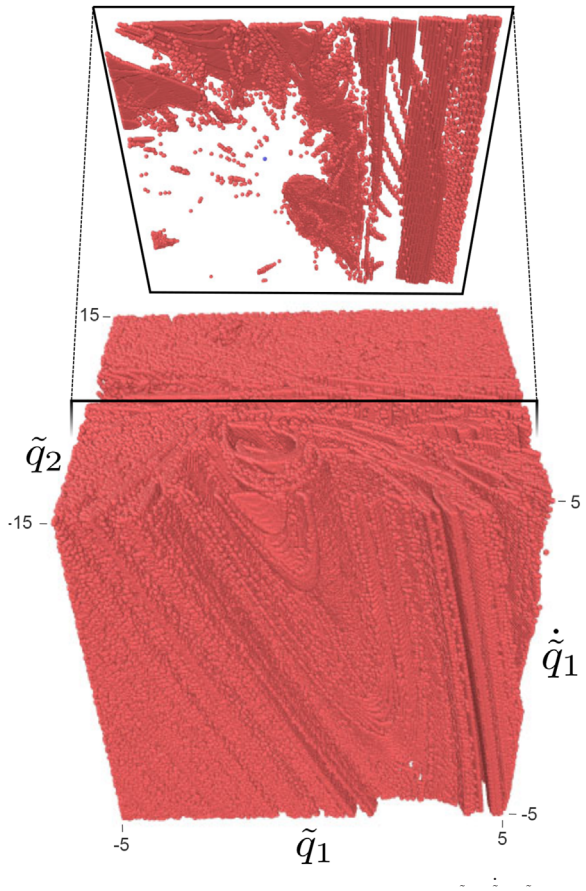

Fig. 8 Three-dimensional section in the space $[q_1, \dot{q}_1, q_2]$ out of the 4D basin of attraction (discretization resolution $400 \times 400 \times 400 \times 400$). The figure reports only the basin for the repulsive motion of the cantilever whereas empty (white) spaces are initial conditions for the attractive solution. Each dot represent the center of the discretized cell of an initial condition. The 3D basin is extracted from the 4D at $[\cdot, \cdot, \cdot, 0.485640]$. Highlighted basin on top is the obtained by slicing among the attractor position in the plane $[q_1, \dot{q}_1]$. The blue dot (light color in the hard copy) is the steady-state attractor of the attractive regime (white basin).

TM-AFM using the MDOF approximation which enables assessment of the contribution of higher eigenmodes. Indeed, it has been demonstrated experimentally that the AFM periodic oscillations are modified by the activation of higher modes of vibration as a consequence of the strong nonlinear interaction $F_{ts}(\bar{z})$ [43]. Again, the influence of a multimode approximation is linked to the higher-order damping coefficients. In other words, only assuming large quality-factors (i.e., low dissipation coefficients) we allow for energy-transfer and higher-modes of vibration to be activated. The MDOF analysis points that the D_2^{att} higher damping coefficients in the attractive region plays only a minor role due the weakness of the

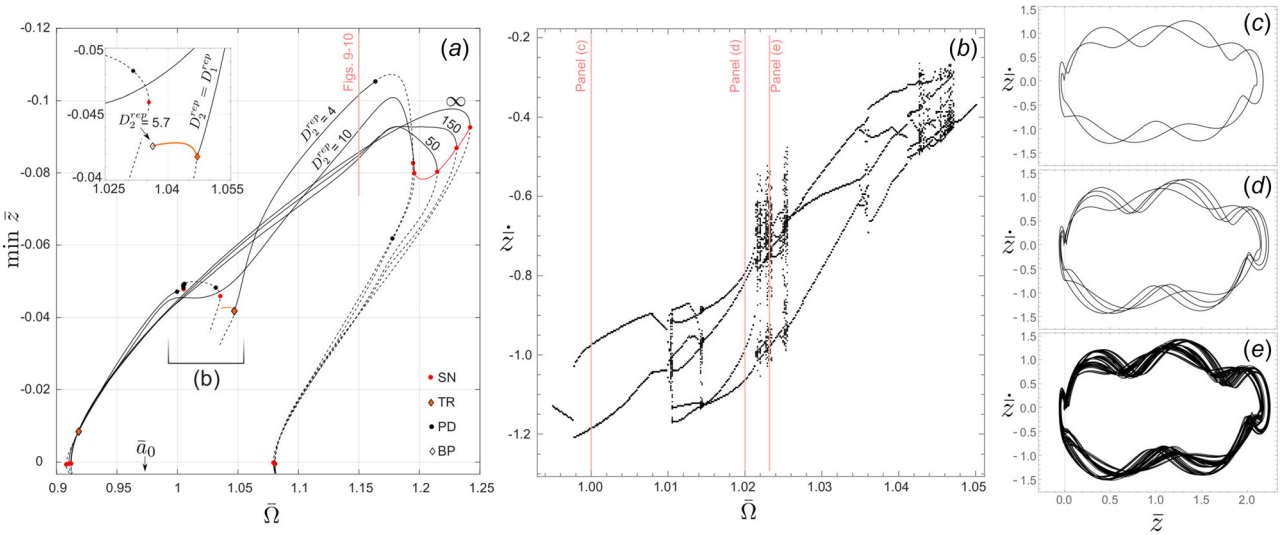

Fig. 7 Dynamical response in the repulsive region approximated with two modes ($n = 2$ in Eq. (5)). Panel (*a*) shows the frequency response for the amplitude-saturated response by varying D_2^{rep}. The inset highlights on the disappearance of the torus bifurcation (empty diamond). Panel (*b*) reports the bifurcation diagram computed via numerical integration. The bifurcation parameter is $0.995 \le \bar{\Omega} \le 1.05$. The span is divided in 300 steps, for each frequency we discard 600 periods and we plot the last 100 dimensionless values of the velocity in the Poincaré map. Panels (*c*)–(*e*) are phase-space portrait at $\bar{\Omega}$=1.00, $\bar{\Omega}$=1.02, $\bar{\Omega}$=1.023, respectively.

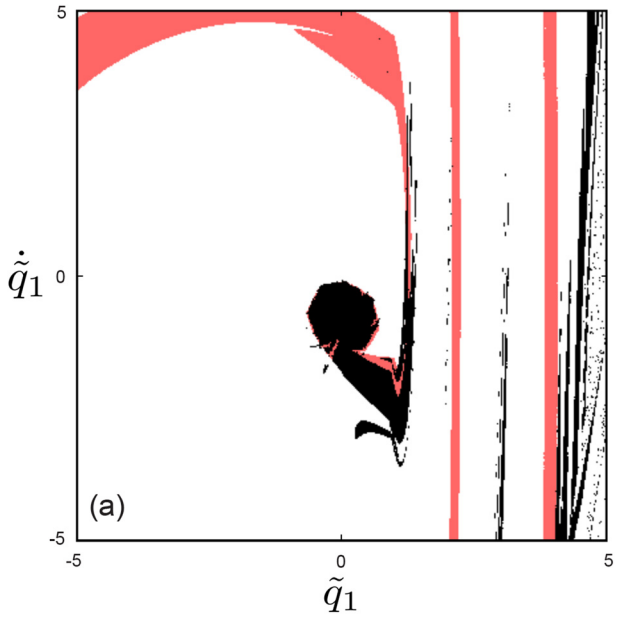

Fig. 9 Basin of attraction employing 1 DOF (red - lighter color in the hard copy) and 2 DOF (black - darker color in the hard copy). Section of the 2D basins in the $[\tilde{q}_1, \dot{\tilde{q}}_1]$ space at $[\cdot, \cdot, -0.028993, 0.485640]$.

interaction. Figure 7(*a*) presents the frequency response by accounting for the second mode of the cantilever while varying the dissipation coefficient of the second mode D_2^{rep}. The red locus of the saddle shows how the 2-DOF model evolves with the dissipation coefficient. When $D_2^{\text{rep}} = \infty$, the response perfectly overlaps with a frequency response curve based on a SDOF approximation. Experimental ongoing investigations are demonstrating that near-vacuum conditions enhance the activation of higher modes while a humid environment damps these contribution. This is in complete agreement with the results obtained via continuation reported in Fig. 7(*a*). The numerical continuation faces problem in the region marked as (b) where branch of periodic trajectories are terminated. In order to proceed and characterize the region beyond torus and period-doubling bifurcations, forward-time numerical simulations are performed to get the steady-state attractors. The bifurcation diagram for $0.995 \leq \bar{\Omega} \leq 1.05$ is plotted in Fig. 7(*b*). It shows series of period doubling bifurcations that generate increased periodicity as the period-2 and -4 motion in Figs. 7(*c*) and 7(*d*), respectively. The PD cascade leads to chaotic motion (see Fig. 7(*e*)) that terminates when period halving bifurcations reinstate the order in the cantilever oscillations. When assuming $D_1 = D_2$ torus bifurcation triggers quasi-periodic motion in the AFM cantilever [22]. This motion can be found for $\bar{\Omega} = 1.046$ in Fig. 7(*b*). The existence of quasi-periodic motion is rather limited as demonstrated by the loci of the TR bifurcation (inset of Fig. 7(*a*)). Windows of complex motion and additional bifurcations are considered a perilous condition in TM-AFM. It assume a high importance since commercial AFM systems build the feedback control loop on the cantilever oscillation signal locked on the primary resonant frequency loosing track of higher oscillations. Thus, phenomena connected to higher modes of vibrations remain hidden to the controller and are impossible to correct by closed-loop control.

The metamorphosis of the frequency response as function of the higher dissipation parameter D_2^{rep} rises doubts regarding the global stability of the AFM cantilever. The goal of assessing the safety of a dynamical system under the global perspective is achieved by evaluating basins of attraction [44]. Computation of basins of attraction is not a slight task if dealing with high-dimensional systems [45–47]. However, despite the involved numerical issues, a multidemensional basin estimates the global safety in the whole set of generalized coordinates. Again, here we fix $n = 2$ to get a 2-DOF approximation and calculate the basin of attraction. To this aim, we span a large set of initial conditions in our initial value problem

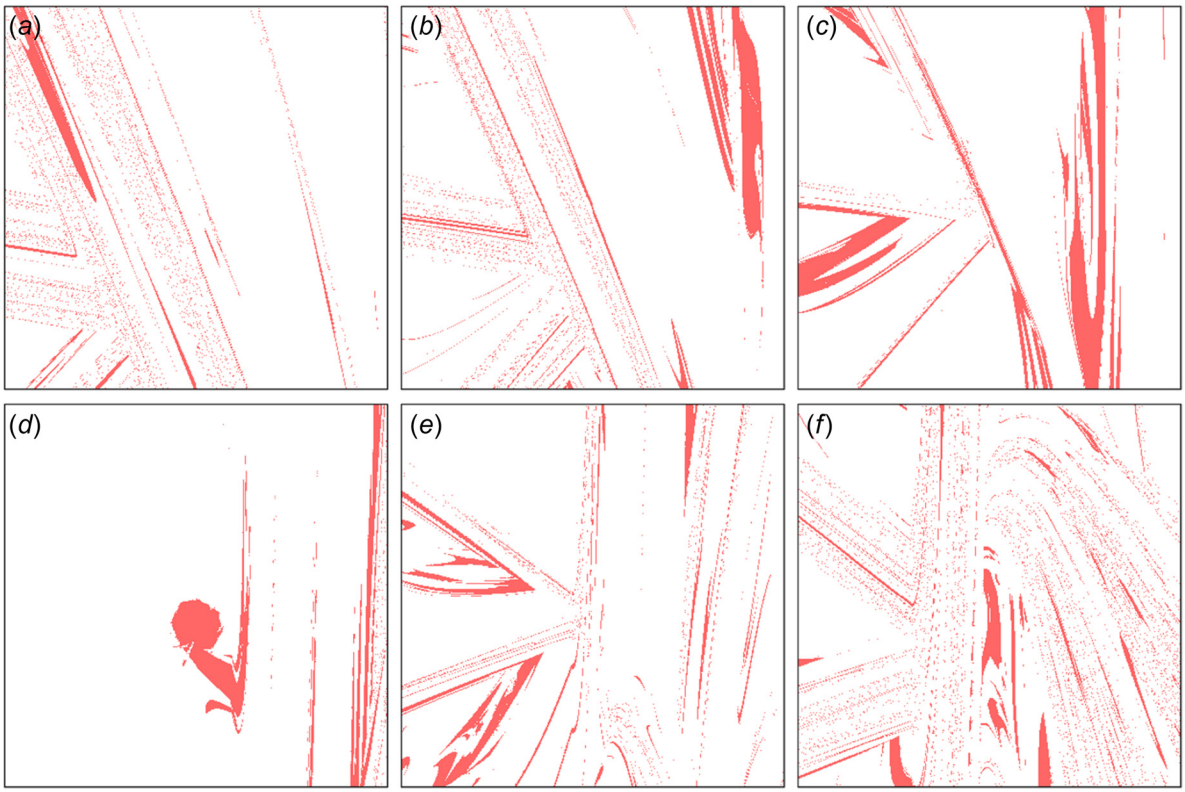

Fig. 10 Two-dimensional sections in the $[\tilde{q}_1, \dot{\tilde{q}}_1]$ space of the 4D basin in the full space $[\cdot, \cdot, \tilde{q}_2, 0.485640]$. The section is extracted at $\tilde{q}_2 = \{-4.39, -2.89, -1.39, 0.11, 1.61, 3.12\}$. Axes limits $\tilde{q}_1 \in [-5, 5]$, $\dot{\tilde{q}}_1 \in [-5, 5]$.

looking for the correlated attractive set. The basin is calculated for the fixed dimensionless frequency $\bar{\Omega} = 1.15$ in proximity of a PD bifurcation as illustrated in Fig. 7(*a*). Since the 2-DOF system under investigation corresponds to a set of 4 ODEs, the dimension of the basin is four. It follows that only 2D/3D sections of the multi-dimensional basin can be plotted out of the set $[\tilde{q}_1, \dot{\tilde{q}}_1, \tilde{q}_2, \dot{\tilde{q}}_2]$. The global analysis unveils the coexistence of two basins, one for the motion in the repulsive regime and other out of the contact far from the sample. A 3D section of the basin for the repulsive solution is shown in Fig. 8. The figure reports in red the initial conditions bringing the AFM in the repulsive region. The empty/white spaces compose the basin relative to the attractive solution. In the figure, the basin is sliced around the period-1 attractor to extract a 2D section. Extracting sections out of multidimensional basin allow for a better interpretation. Figure 9 reports the basin obtained in a SDOF approximation (red/white) and the one obtained by slicing the full 4D basin (black/white). Red-black/white basin refers to the repulsive/attractive attractors. Both basins are in the space of the first generalized coordinate and first generalized velocity, i.e., $[\tilde{q}_1, \dot{\tilde{q}}_1]$. At a glance they do not seem to largely differ and we can comment only on a more accentuated boundary fractalization in the MDOF case. However, if we consider different 2D sections by varying the $\tilde{q}_2$ coordinate in the multidimensional basin we assist to a piercing modification of the global topology. This is illustrated in Fig. 10. Thus, from a practical point of view perturbations affecting the dynamics of the second eigenmode could easily enhance the transition from repulsive to attractive domain, and, remarkably, this happens even without internal resonance coupling the dynamics of the two considered different modes. Finally, we remark that additional DOFs are to be speciffically evaluated case-by-case. The correct number n to be used in Eq. (5) is function of the dissipation mechanisms, i.e., the environment, but also connected to the AFM operation. Gentle tapping could be well represented by a SDOF whereas near vacuum strong tapping sees activation of more than two modes.

5 Conclusions

In this study, the tip-sample interaction in an atomic force microscope operating in tapping mode was examined. Realistic van der Waals/DMT contact forces were used to describe the nonsmooth dynamics. A multimode Galerkin is applied to obtain a system of ODEs that is expressed as a hybrid dynamical system. Numerical continuations of periodic solution have been obtained by making use of a modern bifurcation analysis toolbox. We investigated the amplitude-saturated branch in the repulsive regime as a function of the diverse dissipation mechanisms while the tip is in air or in contact with the sample. The shape and extension of the periodic solution in the repulsive region are receptive to sample properties and to be potentially exploited in dynamical-based identification of specimens in the repulsive region.

By means of a multimode approximation new insights in the nonlinear dynamics have been gained. Higher modes are meaningful to unveil nonregular dynamics region that cannot be captured by a SDOF reduced-order model. Moreover the global analysis carried out with multidimensional basins of attraction suggests that higher eigenmodes could mine the practical stability of the cantilever, even away from internal resonance. These effects cannot be captured by the single mode approximation and underline the need for thorough analyses on the anharmonic cantilever oscillations in TM-AFM. The study based on a multimode perspective provides a twofold opportunity: (i) to exploit the richness of the dynamical scenario in the by MDOF ROM for simultaneous identifications; (ii) to investigate the full response and aim for an augmented control of the atomic microscope that increases stability and reliability.

Data Availability Statement

The datasets generated and supporting the findings of this article are obtainable from the corresponding author upon reasonable request.

References

[1] Gross, L., Mohn, F., Moll, N., Liljeroth, P., and Meyer, G., 2009, "The Chemical Structure of a Molecule Resolved by Atomic Force Microscopy," Science, **325**(5944), pp. 1110–1114.
[2] Rabe, U., Amelio, S., Kopycinska, M., Hirsekorn, S., Kempf, M., Goken, M., and Arnold, W., 2002, "Imaging and Measurement of Local Mechanical Material Properties by Atomic Force Acoustic Microscopy," Surf. Interface Anal., **33**(2), pp. 65–70.
[3] García, R., 2010, *Theory of Amplitude Modulation AFM*, Wiley, NY, pp. 41–57.
[4] García, R., and Pérez, R., 2002, "Dynamic Atomic Force Microscopy Methods," Surf. Sci. Rep., **47**(6–8), pp. 197–301.
[5] San Paulo, A., and García, R., 2000, "High-Resolution Imaging of Antibodies by Tapping-Mode Atomic Force Microscopy: Attractive and Repulsive Tip-Sample Interaction Regimes," Biophys. J., **78**(3), pp. 1599–1605.
[6] Stark, M., Möller, C., Müller, D. J., and Guckenberger, R., 2001, "From Images to Interactions: High-Resolution Phase Imaging in Tapping-Mode Atomic Force Microscopy," Biophys. J., **80**(6), pp. 3009–3018.
[7] Rajabifar, B., Jadhav, J. M., Kiracofe, D., Meyers, G. F., and Raman, A., 2018, "Dynamic AFM on Viscoelastic Polymer Samples With Surface Forces," Macromolecules, **51**(23), pp. 9649–9661.
[8] Chandrashekar, A., Belardinelli, P., Bessa, M. A., Staufer, U., and Alijani, F., 2022, "Quantifying Nanoscale Forces Using Machine Learning in Dynamic Atomic Force Microscopy," Nanoscale Adv., **4**(9), pp. 2134–2143.
[9] Cartagena, A., and Raman, A., 2014, "Local Viscoelastic Properties of Live Cells Investigated Using Dynamic and Quasi-Static Atomic Force Microscopy Methods," Biophys. J., **106**(5), pp. 1033–1043.
[10] García, R., and San Paulo, A., 1999, "Attractive and Repulsive Tip-Sample Interaction Regimes in Tapping-Mode Atomic Force Microscopy," Phys. Rev. B, **60**(7), pp. 4961–4967.
[11] Hashemi, N., Dankowicz, H., and Paul, M. R., 2008, "The Nonlinear Dynamics of Tapping Mode Atomic Force Microscopy With Capillary Force Interactions," J. Appl. Phys., **103**(9), p. 093512.
[12] Zhao, X., and Dankowicz, H., 2006, "Characterization of Intermittent Contact in Tapping-Mode Atomic," ASME J. Comput. Nonlinear Dyn., **1**(2), pp. 109–115.
[13] Chandrashekar, A., Belardinelli, P., Staufer, U., and Alijani, F., 2019, "Robustness of Attractors in Tapping Mode Atomic Force Microscopy," Nonlinear Dyn., **97**(2), pp. 1137–1158.
[14] Rull Trinidad, E., Gribnau, T. W., Belardinelli, P., Staufer, U., and Alijani, F., 2017, "Nonlinear Dynamics for Estimating the Tip Radius in Atomic Force Microscopy," Appl. Phys. Lett., **111**(12), p. 123105.
[15] Davidovikj, D., Alijani, F., Cartamil-Bueno, S. J., van der Zant, H. S. J., Amabili, M., and Steeneken, P. G., 2017, "Nonlinear Dynamic Characterization of Two-Dimensional Materials," Nat. Commun., **8**(1), p. 1253.
[16] Raman, A., Melcher, J., and Tung, R., 2008, "Cantilever Dynamics in Atomic Force Microscopy," Nano Today, **3**(1–2), pp. 20–27.
[17] García, R., and San Paulo, A., 2000, "Dynamics of a Vibrating Tip Near or in Intermittent Contact With a Surface," Phys. Rev. B, **61**(20), pp. R13381–R13384.
[18] Paulo, A. S., and García, R., 2001, "Tip-Surface Forces, Amplitude, and Energy Dissipation in Amplitude-Modulation (Tapping Mode) Force Microscopy," Phys. Rev. B, **64**(19), p. 193411.
[19] Verbiest, G., and Rost, M., 2016, "Resonance Frequencies of Afm Cantilevers in Contact With a Surface," Ultramicroscopy, **171**, pp. 70–76.
[20] Paulo, A. S., and García, R., 2002, "Unifying Theory of Tapping-Mode Atomic-Force Microscopy," Phys. Rev. B, **66**(4), p. 041406.
[21] Lee, S. I., Howell, S. W., Raman, A., and Reifenberger, R., 2003, "Nonlinear Dynamic Perspectives on Dynamic Force Microscopy," Ultramicroscopy, **97**(1–4), pp. 185–198.
[22] Bahrami, A., and Nayfeh, A. H., 2012, "On the Dynamics of Tapping Mode Atomic Force Microscope Probes," Nonlinear Dyn., **70**(2), pp. 1605–1617.
[23] Rützel, S., Lee, S. I., and Raman, A., 2003, "Nonlinear Dynamics of Atomic Force Microscope Probes Driven in Lennard-Jones Potentials," Proc. R. Soc. London. Ser. A, **459**(2036), pp. 1925–1948.
[24] Chandrashekar, A., Belardinelli, P., Lenci, S., Staufer, U., and Alijani, F., 2021, "Mode Coupling in Dynamic Atomic Force Microscopy," Phys. Rev. Appl., **15**, p. 024013.
[25] Herruzo, E. T., Perrino, A. P., and Garcia, R., 2014, "Fast Nanomechanical Spectroscopy of Soft Matter," Nat. Commun., **5**(1), p. 3126.
[26] Hillenbrand, R., Stark, M., and Guckenberger, R., 2000, "Higher-Harmonics Generation in Tapping-Mode Atomic-Force Microscopy: Insights Into the Tip-Sample Interaction," Appl. Phys. Lett., **76**(23), pp. 3478–3480.
[27] Martinez-Martin, D., Herruzo, E. T., Dietz, C., Gomez-Herrero, J., and Garcia, R., 2011, "Noninvasive Protein Structural Flexibility Mapping by Bimodal Dynamic Force Microscopy," Phys. Rev. Lett., **106**(19), p. 198101.
[28] Andreaus, U., Placidi, L., and Rega, G., 2013, "Microcantilever Dynamics in Tapping Mode Atomic Force Microscopy Via Higher Eigenmodes Analysis," J. Appl. Phys., **113**(22), p. 224302.
[29] Bahrami, A., and Nayfeh, A. H., 2013, "Nonlinear Dynamics of Tapping Mode Atomic Force Microscopy in the Bistable Phase," Commun. Nonlinear Sci. Numer. Simul., **18**(3), pp. 799–810.
[30] Derjaguin, B., Muller, V., and Toporov, Y., 1975, "Effect of Contact Deformations on the Adhesion of Particles," J. Colloid Interface Sci., **53**(2), pp. 314–326.
[31] Dankowicz, H., Zhao, X., and Misra, S., 2007, "Near-Grazing Dynamics in Tapping-Mode Atomic-Force Microscopy," Int. J. Non-Linear Mech., **42**(4), pp. 697–709.

[32] Lee, S. I., Howell, S. W., Raman, A., and Reifenberger, R., 2002, "Nonlinear Dynamics of Microcantilevers in Tapping Mode Atomic Force Microscopy: A Comparison Between Theory and Experiment," Phys. Rev. B, **66**(11), p. 115409.
[33] Gotsmann, B., and Fuchs, H., 2001, "Dynamic Force Spectroscopy of Conservative and Dissipative Forces in an al-au(111) Tip-Sample System," Phys. Rev. Lett., **86**(12), pp. 2597–2600.
[34] Dankowicz, H., and Schilder, F., 2013, *Recipes for Continuation*, Computational Science and Engineering, Society for Industrial and Applied Mathematics, Society for Industrial and Applied Mathematics, Philadelphia, PA.
[35] Ahsan, Z., Dankowicz, H., Li, M., and Sieber, J., 2022, "Methods of Continuation and Their Implementation in the Coco Software Platform With Application to Delay Differential Equations," Nonlinear Dyn., **107**(4), pp. 3181–3243.
[36] Páez Chávez, J., Zhang, Z., and Liu, Y., 2020, "A Numerical Approach for the Bifurcation Analysis of Nonsmooth Delay Equations," Commun. Nonlinear Sci. Numer. Simul., **83**, p. 105095.
[37] Belardinelli, P., Lenci, S., and Rega, G., 2018, "Seamless Variation of Isometric and Anisometric Dynamical Integrity Measures in Basins's Erosion," Commun. Nonlinear Sci. Numer. Simul., **56**, pp. 499–507.
[38] Aldridge, J. S., and Cleland, A. N., 2005, "Noise-Enabled Precision Measurements of a Duffing Nanomechanical Resonator," Phys. Rev. Lett., **94**(15), pp. 5–8.
[39] Nayfeh, A., and Balachandran, B., 2008, *Applied Nonlinear Dynamics: Analytical, Computational, and Experimental Methods*, Series in Nonlinear Science, Wiley, Hoboken, NJ.
[40] Misra, S., Dankowicz, H., and Paul, M. R., 2010, "Degenerate Discontinuity-Induced Bifurcations in Tapping-Mode Atomic-Force Microscopy," Phys. D (Amsterdam, Neth.), **239**(1–2), pp. 33–43.
[41] Liao, M., Ing, J., Chávez, J. P., and Wiercigroch, M., 2016, "Bifurcation Techniques for Stiffness Identification of an Impact Oscillator," Commun. Nonlinear Sci. Numer. Simul., **41**, pp. 19–31.
[42] Keyvani, A., Alijani, F., Sadeghian, H., Maturova, K., Goosen, H., and van Keulen, F., 2017, "Chaos: The Speed Limiting Phenomenon in Dynamic Atomic Force Microscopy," J. Appl. Phys., **122**(22), p. 224306.
[43] Stark, M., Stark, R. W., Heckl, W. M., and Guckenberger, R., 2000, "Spectroscopy of the Anharmonic Cantilever Oscillations in Tapping-Mode Atomic-Force Microscopy," Appl. Phys. Lett., **77**(20), pp. 3293–3295.
[44] Rega, G., and Lenci, S., 2015, "A Global Dynamics Perspective for System Safety From Macro- to Nanomechanics: Analysis, Control, and Design Engineering," ASME Appl. Mech. Rev., **67**(5), pp. 50802–50819.
[45] Belardinelli, P., and Lenci, S., 2016, "An Efficient Parallel Implementation of Cell Mapping Methods for MDOF Systems," Nonlinear Dyn., **86**(4), pp. 2279–2290.
[46] Belardinelli, P., and Lenci, S., 2017, "IUTAM Symposium on Nonlinear and Delayed Dynamics of Mechatronic Systems: Improving the Global Analysis of Mechanical Systems Via Parallel Computation of Basins of Attraction," Procedia IUTAM, **22**, pp. 192–199.
[47] Andonovski, N., and Lenci, S., 2020, "Six-Dimensional Basins of Attraction Computation on Small Clusters With Semi-Parallelized Scm Method," Int. J. Dyn. Control, **8**(2), pp. 436–447.